Atmospheric
Chemistry
and Physics

Chemical and meteorological influences on the lifetime of NO_3 at a semi-rural mountain site during PARADE

N. Sobanski[1], M. J. Tang[1,a], J. Thieser[1], G. Schuster[1], D. Pöhler[2], H. Fischer[1], W. Song[1], C. Sauvage[1], J. Williams[1], J. Fachinger[3], F. Berkes[4,b], P. Hoor[4], U. Platt[2], J. Lelieveld[1], and J. N. Crowley[1]

[1]Division of Atmospheric Chemistry, Max-Planck-Institut für Chemie, Mainz, Germany
[2]Institute of Environmental Physics, University of Heidelberg, Heidelberg, Germany
[3]Division of Particle Chemistry, Max-Planck-Institut für Chemie, Mainz, Germany
[4]Institute for Atmospheric Physics, Johannes Gutenberg University Mainz, Mainz, Germany
[a]present address: Chemistry Department, University of Iowa, Iowa City, USA
[b]present address: Institute of Energy and Climate, Forschungszentrum Jülich, Jülich, Germany

Correspondence to: J. N. Crowley (john.crowley@mpic.de)

Abstract. Through measurements of NO_2, O_3 and NO_3 during the PARADE campaign (PArticles and RAdicals, Diel observations of mEchanisms of oxidation) in the German Taunus mountains we derive nighttime steady-state lifetimes (τ_{ss}) of NO_3 and N_2O_5. During some nights, high NO_3 (~ 200 pptv) and N_2O_5 (~ 1 ppbv) mixing ratios were associated with values of τ_{ss} that exceeded 1 h for NO_3 and 3 h for N_2O_5 near the ground. Such long boundary-layer lifetimes for NO_3 and N_2O_5 are usually only encountered in very clean/unreactive air masses, whereas the PARADE measurement site is impacted by both biogenic emissions from the surrounding forest and anthropogenic emissions from the nearby urbanised/industrialised centres. Measurement of several trace gases which are reactive towards NO_3 indicates that the inferred lifetimes are significantly longer than those calculated from the summed loss rate. Several potential causes for the apparently extended NO_3 and N_2O_5 lifetimes are examined, including additional routes to formation of NO_3 and the presence of a low-lying residual layer. Overall, the most likely cause of the anomalous lifetimes are related to the meteorological conditions, though additional NO_3 formation due to reactions of Criegee intermediates may contribute.

1 Introduction

NO_3 and N_2O_5 are key species in the chemical removal of NO_x and of several hydrocarbons at night (Wayne et al., 1991; Atkinson and Arey, 2003). Traditionally, NO_3 is considered to be formed mainly by the reaction of NO_2 with O_3 (Reaction R1) with negligible contributions e.g. from reaction between OH and HNO_3 (Reaction R2) or the photolysis of halogen nitrates ($XONO_2$), where X may be Br or Cl (Reaction R3). N_2O_5 is produced in an association reaction between NO_3 and NO_2 (Reaction R4a), with which it is in thermal equilibrium (Reactions R4a, b).

$$NO_2 + O_3 \rightarrow NO_3 + O_2 \tag{R1}$$
$$OH + HNO_3 \rightarrow NO_3 + H_2O \tag{R2}$$
$$XONO_2 + h\nu \rightarrow NO_3 + X \tag{R3}$$

$$NO_2 + NO_3 + M \rightarrow N_2O_5 + M \tag{R4a}$$
$$N_2O_5 + M \rightarrow NO_3 + NO_2 + M \tag{R4b}$$

The production rate of NO_3 is therefore usually assumed to be the product of the NO_2 and O_3 concentrations and the rate constant (k_1):

$$P(NO_3) = k_1[NO_2][O_3]. \tag{1}$$

In general, equilibrium between N$_2$O$_5$, NO$_3$ and NO$_2$ is reached rapidly following sunset and holds until sunrise (Brown et al., 2003). During the day, NO$_3$ is photolysed (with a lifetime of a few seconds) to give NO$_2$ + O (Reaction R5a, ∼ 90 %) or NO + O$_2$ (Reaction R5b, ∼ 10 %) (Johnston et al., 1996) and also reacts quickly with NO (Reaction R6) so that NO$_3$ and N$_2$O$_5$ mixing ratios are usually below the detection limit of most instruments. During the night, in the absence of light to regenerate it from NO$_2$ (Reaction R7) and with sufficient distance from emissions sources, NO levels approach 0 (due to Reaction R8) and NO$_3$ and N$_2$O$_5$ can accumulate in the atmosphere.

$$NO_3 + h\nu \rightarrow NO_2 + O \qquad (R5a)$$

$$NO_3 + h\nu \rightarrow NO + O_2 \qquad (R5b)$$

$$NO_3 + NO \rightarrow 2NO_2 \qquad (R6)$$

$$NO_2 + h\nu \rightarrow NO + O \qquad (R7)$$

$$NO + O_3 \rightarrow NO_2 + O_2 \qquad (R8)$$

The mechanism and rate of removal of NO$_3$ and N$_2$O$_5$ from the atmosphere depend on the type of air mass. In areas impacted by local anthropogenic activity, NO can be a major sink of NO$_3$. The rate constant for this reaction of 2.6×10^{-11} cm^3 molecule^{-1} s^{-1} at 298 K (Atkinson et al., 2004) results, for example, in a chemical lifetime for NO$_3$ of about 16 s in the presence of 100 pptv of NO. NO$_3$ mixing ratios measured in situ at ground level in cities are sometimes low due to the high mixing ratio of NO. However, a few tens of kilometres downwind of urban areas or several tens of metres aloft, where [NO] can be significantly lower due to reduced mixing of ground-level emissions and titration by O$_3$, NO$_3$ mixing ratios can reach up to several hundred pptv and N$_2$O$_5$ up to a few ppbv (Asaf et al., 2009; Brown et al., 2009). Downwind of industrial activity, especially that related to petroleum production and storage, observed NO$_3$ lifetimes are limited by the presence of reactive hydrocarbons (Geyer et al., 2003; Stutz et al., 2010; Brown et al., 2011; Crowley et al., 2011).

In rural and forested environments, NO can be emitted from soils but is in general much less concentrated than in urban areas, and its mixing ratio is often close to 0 at night. In these environments, biogenic volatile organic compounds (BVOCs) can contribute a substantial fraction of the NO$_3$ reactivity. Unsaturated BVOCs such as monoterpenes have large rate constants for reaction with NO$_3$, e.g. ∼ 10^{-11} cm^3 molecule^{-1} s^{-1} for limonene and 10^{-12} cm^3 molecule^{-1} s^{-1} for α-pinene and β-pinene (Atkinson and Arey, 2003). In heavily forested areas with high monoterpene emission rates, NO$_3$ lifetimes may be reduced to a few tens of seconds (Rinne et al., 2012; Mogensen et al., 2015), resulting in efficient conversion of NO$_x$ to organic nitrates and formation of secondary organic aerosol (Hallquist et al., 1999; Fry et al., 2014).

In the absence of any known, significant gas-phase reaction, the main sink of N$_2$O$_5$ at night is heterogeneous hydrolysis on aqueous aerosols, clouds and surfaces. The formation of particle-phase HNO$_3$ by this route results in repartitioning of NO$_x$ from the gas to the condensed phase. Deposition of the particle nitrate formed is a substantial, permanent loss process for NO$_x$, resulting in reduced rates of photochemical O$_3$ production. Furthermore, if the aerosol particles contain chloride, the uptake of N$_2$O$_5$ can result in release of ClNO$_2$ and subsequently Cl atoms, which may enhance the rates of oxidation of hydrocarbons (Behnke et al., 1997; Osthoff et al., 2008; Bertram and Thornton, 2009; Thornton et al., 2010; Sarwar et al., 2012). The N$_2$O$_5$ uptake coefficient (overall efficiency of transfer from gas to particle phase) is largest for aqueous aerosols but depends on the composition of the aerosol (nitrate, sulfate and organic content) and humidity and possible organic coatings (Riemer et al., 2009) and is thus highly variable in time and space. Losses of NO$_3$ to aerosol or other surfaces are generally considered to be minor compared to its gas-phase losses and indirect losses via N$_2$O$_5$ uptake. In environments such as clean marine air masses where reactive partners for NO$_3$ are absent, lifetimes can become large and N$_2$O$_5$ losses to aerosol or surfaces may control the NO$_3$ levels via the equilibrium (Reactions R4a, b) (Heintz et al., 1996; Martinez et al., 2000).

Over the continents during the night, when the earth's surface does not receive energy by solar radiation, it cools down and the convective mixing which usually takes place during the day stops. This results in formation of a shallow, weakly mixed nocturnal boundary layer, with strong vertical stratification. Under such conditions, pronounced vertical gradients in NO$_3$ and N$_2$O$_5$ mixing ratios have been observed (von Friedeburg et al., 2002; Stutz et al., 2004; Brown et al., 2007) with ground-level emissions (both biogenic and anthropogenic) often resulting in lower NO$_3$ and N$_2$O$_5$ lifetimes, with cleaner air aloft (e.g. in the residual layer or free troposphere) often resulting in higher values. In all these different environments, the emission/formation rates of VOCs and aerosols and subsequent mixing are thus the key parameters controlling the NO$_3$ and N$_2$O$_5$ lifetimes.

In this paper, we describe a subset of an extensive suite of measurements obtained in the PARADE (PArticles and RAdicals, Diel observations of mEchanisms of oxidation) campaign (August–September 2011) at the top of a ∼ 825 m high mountain situated between an urbanised flatland area and a forested mountainous area. A first campaign at this site (Crowley et al., 2010) during May 2009 found maximum NO$_3$ lifetimes of 10 to 15 min with mixing ratios up to 50 pptv for NO$_3$ and 500 pptv for N$_2$O$_5$. From the results of this first campaign it was concluded that at near-zero nighttime NO mixing ratios, the NO$_3$ lifetime was most likely controlled by emissions of BVOCs, which were, however, not measured. The heterogeneous loss of N$_2$O$_5$ was found to be only of limited importance in controlling NO$_3$ lifetimes. During PARADE, several hydrocarbons, both biogenic and an-

thropogenic, were measured as well as NO and also aerosol surface area (ASA) and chemical composition. We compare NO$_3$ lifetimes calculated using a steady-state approximation (based on the NO$_3$ production rate and mixing ratio) with those derived from the summed reactivity of individual trace gases and surfaces. For several campaign nights, we found that the steady-state lifetime significantly exceeded the lower limit of the NO$_3$ lifetime calculated from the summed reactivity and investigate potential causes of this.

2   Campaign location and measurement techniques

2.1   Site description

The PARADE campaign took place at the Taunus Observatory located on top of the Kleiner Feldberg mountain (50.22° N, 8.45° E) 825 m above sea level (a.s.l.). Local sites at the base of the mountains are at elevations of 120 ± 50 m. The station is used permanently by the environment and geological agency of the state of Hessen (HLUG) and the German weather service (DWD). The site has already been described (Handisides, 2001; Crowley et al., 2010), and only a short summary is given below. Directly (1–2 km) to the north-north-east and the south-east of the site are two similarly high mountains (Großer Feldberg at 878 m and Altkoenig at 798 m a.s.l.). The area in the north-west to north-east sector may be described as a relatively sparsely populated, partially forested rural region, whereas the south-west to south-east sector contains significant urban infrastructure including the densely populated cities of Frankfurt (~ 20 km to the south-east) and Mainz and Wiesbaden (20–30 km to the south-west). The site is directly surrounded (100 m radius) by a mix of coniferous trees (mainly spruce) and shrubs. Within a radius of 5 km from the site, the region is dominated by forest (coniferous, broad-leaved and mixed), especially to the north-east which has the lowest contribution from local agriculture and urban emissions. This is displayed in the land-use pie charts found in Fig. S1 in the Supplement. The same figure indicates that over a distance of 50 km, a significant fraction ($\sim 50\%$) of the land area is used for agriculture.

The largest urban influence is found in the south-east sector for both 5 and 50 km distances to the site. In the northern sectors, the closest cities are located between 60 and 90 km away from the site and are significantly less populated than Frankfurt, Mainz and Wiesbaden. The heavily populated and industrialised *Ruhrgebiet* is about 130 km towards the north-west.

During the PARADE campaign, most instruments were located in the permanent laboratory facilities at the site. A platform on top of the building was used to house some instruments and the inlets outside at a height (from the ground) of about 8 m. Measurements central to this study (NO, NO$_2$, NO$_3$, N$_2$O$_5$, O$_3$, VOCs) were sampled via co-located in-

Table 1. Instruments deployed during PARADE.

Species	Instrument	Inlet position
NO$_3$ and N$_2$O$_5$	CRDS	Tower
NO$_3$	LP-DOAS	Roof*
NO$_2$	CRDS	Tower
NO	CLD	Tower
VOCs	GC-MS/GC-FID	Tower
O$_3$	AirPointer	MoLa
Aerosol surface area	FMPS/APS	MoLa

* The telescope of the LP-DOAS set-up was located on the roof, about 2 m below the inlets of the point measurements. The retroreflectors were at different heights at a distance of ~ 1.5 km towards the north (see Sect. 2.2.4).

lets (< 5 m horizontal separation, < 1 m vertical separation). Aerosol measurements were made from a mobile laboratory (MoLa) (Drewnick et al., 2012) with its inlet at 10 m height, about 15 m distant from the main building. The instruments deployed are listed in Table 1, operational details, measurement uncertainties and detection limits are given in the next section. The MoLa also provided meteorological data (wind speed, wind direction, temperature, pressure relative humidity (RH) and global radiation) at 1 s resolution. The values were in generally good agreement with the lower frequency data sets reported by the DWD and HLUG.

2.2   Instrumentation

Below, we describe the instruments (and their overall uncertainties) used to make the critical measurements related to the calculation of NO$_3$ lifetimes. NO$_2$ and O$_3$, important for calculation of NO$_3$ production rates, were measured by multiple instruments, with good agreement. A comparison of three NO$_2$ data sets, including the one used here, is described in Thieser et al. (2016). Several O$_3$ data sets agreed to within about 10 % and the choice of data set for e.g. NO$_2$ or O$_3$ would not change the conclusions of this work.

2.2.1   NO$_2$, NO$_3$ and N$_2$O$_5$ measurements by cavity ring-down spectrometer (CRDS)

The two-channel thermal dissociation CRDS measuring NO$_3$ and N$_2$O$_5$ was deployed at this site during a previous campaign (Schuster et al., 2009; Crowley et al., 2010). Briefly, the CRDS uses a laser diode tuned to 662 nm to directly measure NO$_3$ in one channel at ambient temperature and the sum of (NO$_3$ + N$_2$O$_5$) in a second channel which is held at ~ 100 °C, converting N$_2$O$_5$ to NO$_3$ (plus NO$_2$). Zeroing is performed by addition of NO (Reaction R6). The mixing ratio of N$_2$O$_5$ is then calculated from the difference in mixing ratios observed in each cavity. The CRDS instrument was located outside on the platform on top of the building in order to reduce inlet loss of NO$_3$. Air is drawn through a 1 m length of 0.5 in. (OD) PFA tube at 50 standard L min^{-1} and sampled (18 standard L min^{-1}) from the centre of the flow

via 0.25 in. PFA tubing into the two cavities of the CRDS. This set-up keeps inlet residence times short (≈ 0.1 s) and also helps avoid sampling of coarse particles and droplets. Corrections were applied to account for the losses of NO$_3$ on the filters, on the walls of the automatic filter changer and during passage through the cavities. The overall NO$_3$ transmission was ~ 68 % (Crowley et al., 2010). The instrument detection limit was 2 pptv in 1 s for NO$_3$ and approximately 5 pptv for N$_2$O$_5$. The total uncertainty was ~ 15 % for both NO$_3$ and N$_2$O$_5$, with the largest contributions arising from uncertainty in the NO$_3$ cross section (Orphal et al., 2003; Osthoff et al., 2007) and NO$_3$ losses.

During PARADE, NO$_2$ was measured using several instruments. We use data obtained using CRDS with a 405 nm diode laser as recently described in detail (Thieser et al., 2016). The instrument was zeroed using dry, synthetic air and corrections were made for humidity differences between the zero air and ambient. Typical ring-down times were ~ 30 µs and the instrument has a detection limit for NO$_2$ of ≈ 20 pptv in 1 min and an accuracy of 6 % where the dominant contribution is uncertainty in the NO$_2$ cross sections (Voigt et al., 2002).

2.2.2 VOC measurement by GC

VOCs were measured using two gas-chromatographic instruments with a mass spectrometer (GC-MS) and a flame ionisation detector (GC-FID). The GC-MS measured biogenic and aromatic hydrocarbons with online adsorption/thermal desorption (Markes International) connected to a gas chromatograph (Agilent GC 6890A) and a mass selective detector (Agilent MSD 5973 inert). The time resolution was ~ 1 h (35 min sampling time), and detection limits were around 1 pptv with an uncertainty of 10–15 %.

The GC-FID measured non-methane hydrocarbons (NMHC) using two coupled gas chromatographs (GC 5000 VOC and GC 5000 BTX; AMA instruments, Ulm, Germany). GC 5000 VOC was used for measurement of C2–C6 NMHCs and BTX for C6–C12. The detection limits ranged from 1 to 5 pptv, exceptions being ethane, ethene, propene, benzene and toluene with values of 8, 16, 9, 14 and 48 pptv respectively. The GC-FID was calibrated using a multi-gas mixture (National Physical Laboratory). Total uncertainty is close to 10 % for most trace gases with the exception of 1-pentane (15 %). The time resolution of the measurement is 60 min and the mixing ratio represents an average over a sampling period of 20 min.

2.2.3 NO, O$_3$ and CO$_2$

NO measurements were made with a modified commercial chemiluminescence detector (CLD 790 SR). Operation of this instrument during the PARADE campaign has recently been described (Li et al., 2015). The detection limit for this instrument is 4 pptv in 2 s with a total uncertainty of 4 %. The

O$_3$ data set used in this work was obtained by a commercial AirPointer from Recordum Messtechnik GmbH. It was located in the MoLa and has a detection limit of ~ 1 ppbv (Drewnick et al., 2012) and an accuracy of 5 %. The O$_3$ inlet was situated a few metres above the MoLa, itself located 15 m metres away from the main tower. CO$_2$ was measured using non-dispersive differential broadband infrared absorption (LICOR 6262).

2.2.4 NO$_2$, O$_3$ and NO$_3$ measurements by long-path differential absorption spectroscopy (LP-DOAS)

In addition to the co-located point measurements described above, NO$_2$, O$_3$ and NO$_3$ were also measured by LP-DOAS over a light path of ~ 3 km. The telescope was situated on the same roof as the CRDS instruments (835 m a.s.l.) and was connected with a glass fibre to the laboratory where the light source, spectrometer and other components were located. Three reflectors were positioned at different heights (896.5, 927 and 959 m a.s.l.) to the north-north-east of the telescope on a tower at the Großer Felberg mountain (see Sect. 2.1) at a distance of 1.48 km from the light source. A fourth reflector was positioned on the Großer Feldberg mountainside at a distance of 1.23 km from the light source at 872 m a.s.l. A schematic showing the light paths in relation to the site topography is shown later when we discuss the results. The overall measurement accuracies are 2, 2 and 10 % for NO$_2$, O$_3$ and NO$_3$ respectively and are dominated by uncertainties in the absorption cross sections used.

2.2.5 Particle properties

Particle size information was obtained using MoLa instruments (see above). A fast mobility particle sizer (FMPS 3091, TSI, Inc.) and an aerodynamic particle sizer (APS 3321, TSI, Inc.) as well as an optical particle counter (OPC 1.109, Grimm) covered a particle size range from 5.6 nm to 32 µm. Aerosol was sampled at ambient RH and no correction was applied for hygroscopic growth. The ASA used for calculating rates of trace gas uptake was calculated from the combined FMPS and APS data sets or from the FMPS data alone (5–9 September). Generally, the bulk of the surface area (> 75 %) was found in particles of diameter < 450 nm as measured by the FMPS.

2.2.6 Radiosoundings

The planetary boundary-layer height was determined from radiosondes (GRAW, DFM-06), measuring temperature, relative humidity and position as already described for this campaign (Berkes et al., 2015). Each day, 4 to 10 radiosondes were launched from the summit of the Kleiner Feldberg starting approximately 1 h before sunrise and ending 1 h after sunset. From these data, the potential temperature was calculated and used to determine the type of the boundary layer (stable, neutral, turbulent).

3 Results and discussion

3.1 Meteorological conditions

During the 25 days of the PARADE campaign, the meteorological conditions were quite variable (see Fig. 1). As previously outlined (Phillips et al., 2012), the campaign can be separated broadly into three periods which are associated with different air-mass origins and the arrival of cold fronts. The first part of the campaign from 15 August to 26 August was characterized by a relatively high temperature (up to 25 °C) during the day and a variable day-to-day humidity and wind direction. The air originated from the sector between south and west, and back trajectory calculations using HYSPLIT (Draxler and Rolph, 2011) showed that it was located over the continent during the previous 48 h. Exceptions to this pattern occurred on a few days when air masses passed over the English Channel. The marine influence could be traced through the presence of enhanced ClNO$_2$ (measured using chemical ionisation mass spectrometry) during the night and early morning (Phillips et al., 2012).

The arrival of a cold front originating from the Atlantic on the evening of the 26 August marks the beginning of the second period of the campaign. Immediately following the arrival of this front, the daytime temperature decreased approximately by 10 °C and from 26 to 27 August the relative humidity was close to 100 % and the mountaintop was frequently in clouds. The average daily temperature then slowly increased to reach 20 °C on 3 September in the afternoon. Back trajectories of 48 h showed that from 28 August to 1 September the air was influenced by the Atlantic and the Benelux region. From 1 to 3 September, the 48 h air-mass origin was much closer to the site and stayed over the European continent. The arrival of another front on the evening of 2 September caused the temperature to drop again by 5 °C. Until the end of the campaign, the air originated from the UK and was characterised by low levels of solar radiation and high humidity as the mountaintop was frequently in clouds and fog.

3.2 NO$_2$, NO$_3$ and N$_2$O$_5$ mixing ratios

The NO$_3$, N$_2$O$_5$ and NO$_2$ times series as well as that of O$_3$, NO and ASA are shown in Fig. 2. The mixing ratios of all measured nitrogen species were highly variable due to the close proximity of anthropogenic activity and its spatial/temporal heterogeneity (Crowley et al., 2010; Phillips et al., 2012). NO$_2$ mixing ratios were well above the detection limit during the whole campaign and ranged from 0.5 to more than 20 ppbv, with a campaign average of 2.7 ppbv during the day and 2.6 ppbv during the night. The highest, plume-like values of > 15 ppbv were spread over time periods of a few hours, occurred both day and night and were associated with polluted air masses arriving from the south-east (direction of Frankfurt). During passage of the cold fronts (vertical,
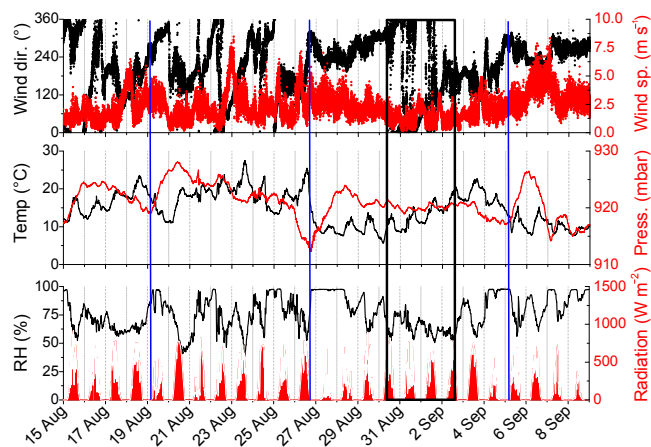

Figure 1. Meteorological parameters measured during the PARADE campaign. The vertical blue lines represent the arrival of cold fronts. The black box corresponds to the time period in which the longest NO$_3$ steady-state lifetimes were measured.
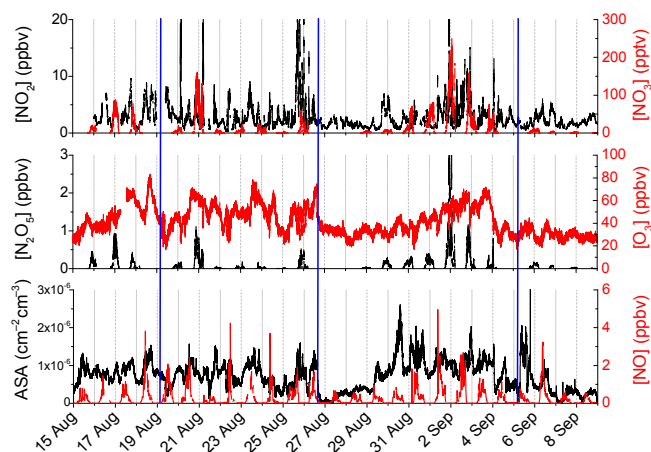

Figure 2. NO$_2$, NO$_3$, N$_2$O$_5$, O$_3$ and NO volume mixing ratios and aerosol surface area (ASA) measured during the PARADE campaign. The vertical, blue lines represent the arrival of cold fronts.

blue lines in Fig. 2) the mountaintop was often in cloud with measured relative humidity close to 100 %. No N$_2$O$_5$ or NO$_3$ could be detected on these nights and O$_3$ levels were reduced to background levels of ∼ 25 ppbv during the following days. The low levels of solar radiation and photochemical activity reduced the maximum daytime mixing concentrations of NO to ∼ 0.5 ppbv.

As NO$_2$ is necessary for the formation of NO$_3$ and N$_2$O$_5$ (Reactions R1 and R4) and also because high levels are indicative of more polluted air masses which are usually associated with shorter NO$_3$ lifetimes, we examine the dependence of NO$_2$ on the local meteorological situation in more detail. A conventional wind rose is displayed in Fig. 3a; in Fig. 3b we plot the relative count frequency of the NO$_2$ mixing ratios indexed against wind direction. The north-east sec-
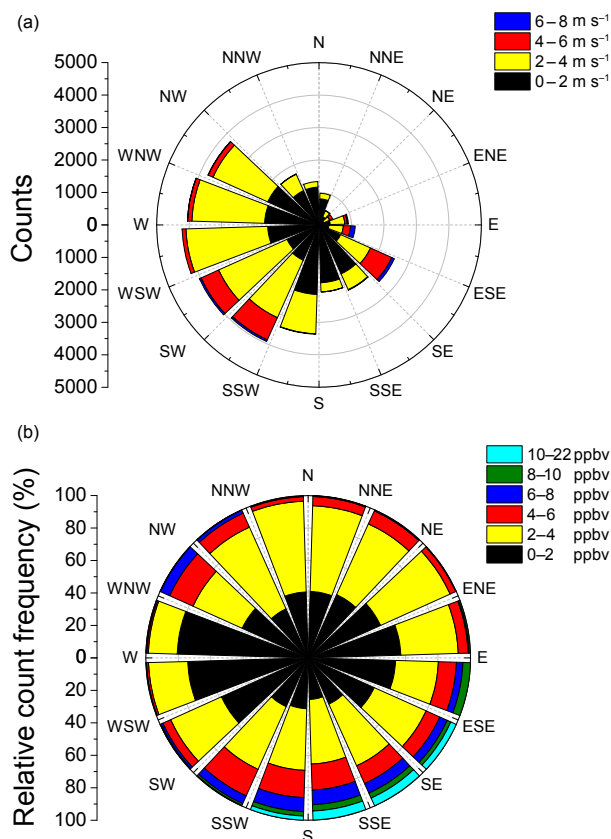
Figure 3. (a) Wind rose indicating the predominant wind direction and speeds throughout the campaign. **(b)** Relative count frequency of NO_2 mixing ratios against wind direction. Mixing ratios higher than 10 ppbv were encountered only for wind directions between east-south-east and south-south-west, reflecting the impact of the major local urban centres.

tor was the least represented with a time coverage of just 6 h. The most frequently encountered wind direction was west (≈ 200 h) but it is also where low NO_2 mixing ratios (< 2 ppbv, in black) were most frequently encountered. The sector east to south-south-west was characterised by frequent high NO_2 mixing ratios. It is the only sector which was associated with NO_2 mixing ratios greater than 10 ppbv, which reflects emissions originating from the three local cities of Frankfurt, Mainz and Wiesbaden. High NO_x levels measured in this sector were associated with the highest levels of anthropogenic hydrocarbons such as toluene.

[NO_3] and [N_2O_5] were highly variable during a single night and also from one night to the next, ranging from below the detection limit to 250 pptv for NO_3 and 3 ppbv for N_2O_5, which is significantly greater than previously measured at this site (Crowley et al., 2010). Precipitation periods were associated with [NO_3] and [N_2O_5] below the detection limit, which is likely a result of N_2O_5 uptake to droplets. The high variability in both [NO_3] and [N_2O_5] is partly due to the variability in their production rate. Figure 4 plots the

mixing ratio of NO_3 (measured at night and at relative humidity lower than 97 %) and its production rate ($P(NO_3)$, in pptv s^{-1}; Fig. 4b) as calculated using Eq. (1) against the local wind direction. Both production rate and mixing ratio of NO_3 show higher values for air masses coming from the Frankfurt and the Mainz/Wiesbaden sectors.

3.3　NO_3 and N_2O_5 lifetimes

The steady-state method for estimating the lifetime of NO_3 is based on the assumption that, after a certain time following sunset, the NO_3 and N_2O_5 concentrations in a single air-mass build-up to a quasi-constant value. Steady state is reached when the sum of direct and indirect loss rate constants of NO_3, $L(NO_3)$ in s^{-1}, balances its production rate, $P(NO_3)$, so that

$$[NO_3]_{ss} = \frac{P(NO_3) + T_{in}(NO_3)}{L(NO_3) + T_{out}(NO_3)}, \tag{2}$$

where $P(NO_3)$ and $L(NO_3)$ are terms for NO_3 chemical formation and loss respectively and $T_{in}(NO_3)$ and $T_{out}(NO_3)$ represent the influence of transport of NO_3. Generally, the terms $T_{in}(NO_3)$ and $T_{out}(NO_3)$ are regarded as insignificant for radical species with chemical lifetimes on the order of minutes rather than hours or days. The simpler form, Eq. (3), for the steady-state approximation has therefore been used frequently in analysing NO_3 measurements (Noxon et al., 1980; Platt et al., 1980; Allan et al., 1999) and has been examined in detail (Brown et al., 2003). At steady state, the NO_3 lifetime (τ_{ss}) is then

$$\tau_{ss}(NO_3) = \frac{[NO_3]}{k_1[NO_2][O_3]} = \frac{1}{L_{ss}(NO_3)}. \tag{3}$$

The term $L_{ss}(NO_3)$ is the loss term of NO_3 corresponding to the steady-state lifetime. The loss term $L(NO_3)$ is the sum of processes removing NO_3 and is often simplified as in Eq. (4):

$$L(NO_3) \approx k_6[NO] + \sum([VOC]_i k_i)$$
$$+ 0.25 K_{eq}[NO_2]\, \bar{c}\, ASA\, \gamma_{N_2O_5}, \tag{4}$$

where k_6 is the rate constant for Reaction (R6) (2.6×10^{-11} cm³ molecule^{-1} s^{-1} at 298 K; Atkinson et al., 2004) and K_{eq} is the equilibrium constant describing the relative concentrations of NO_3 and N_2O_5 under equilibrium for any given NO_2 concentration and temperature and is given by $K_{eq} = k_4/k_{-4}$. $\bar{c}$ is the mean thermal velocity of N_2O_5, k_i is the rate constant for reaction of NO_3 with a VOC, and $\gamma_{N_2O_5}$ is the uptake coefficient for N_2O_5 to aerosol with particle ASA (cm² cm^{-3}). Expressions (3) and (4) ignore loss of NO_3 via heterogeneous uptake and loss of N_2O_5 via gas-phase reactions, both of which are generally considered negligible, and consider NO_3 production path through oxidation of NO_2 by O_3 only. Later, we shall discuss the potential impact of other NO_3 production pathways.
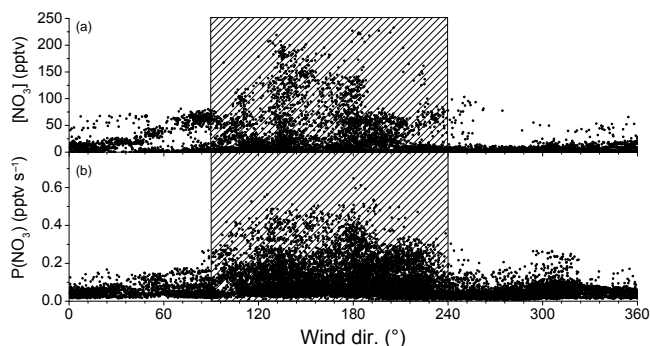
Figure 4. [NO$_3$] and NO$_3$ production rate, P(NO$_3$) from Reaction (R1), vs. wind direction. The grey areas correspond to the Frankfurt–Mainz–Wiesbaden sector. Temperature-dependent rate constants (NO$_2$ + O$_3$), used to calculate the NO$_3$ production term, were taken from an evaluation of kinetic data (Atkinson et al., 2004).

Implicit to this analysis is the assumption that steady state is achieved when the air mass reaches the measurement site. The strongest local sources of NO$_2$ and O$_3$ are likely to be the urban centres of Frankfurt, Mainz and Wiesbaden, all ~ 20 km distant in the southern sectors. As outlined above, there are no close, strong, continuous sources of anthropogenic pollution in the northern sectors. The NO$_3$ production rate as a function of wind direction in Fig. 4 confirms that the whole northern sector is relatively low in NO$_3$ precursors.

With typical wind speeds of between 2 and 5 m s^{-1} the transport times are at least 1 h from the major pollution sources. The time required to achieve steady state depends on the NO$_3$ production term and the overall loss frequency and is shorter when P(NO$_3$) is low and the removal rate high. Numerical simulations were performed to test the validity of the steady-state approximation (Brown et al., 2003) and details are given in the Supplement (Fig. S2). The results indicate that achievement of steady state can indeed take longer than 1 h, when NO$_3$ lifetimes are long, especially when considering air masses with high NO$_2$ and O$_3$ e.g. as occasionally encountered from the southern sectors. During the first hours of nighttime, use of Eq. (3) may thus result in *underestimation* of the steady-state lifetime of NO$_3$.

The NO$_3$ lifetime can also be calculated from the production rate of NO$_3$ and the time derivatives of [NO$_3$] and [N$_2$O$_5$] as in Eq. (5) and thus does not require steady state to have been acquired (McLaren et al., 2010). The lifetime calculated via derivatives, τ_{DER}(NO$_3$), is given by

$$\tau_{DER}(NO_3) = \frac{[NO_3]}{k_1[NO_2][O_3] - \frac{d[NO_3]}{dt} - \frac{d[N_2O_5]}{dt}}. \quad (5)$$

As in the steady-state approximation, this method assumes that only chemical losses impact on NO$_3$ and N$_2$O$_5$ mixing ratios (negligible transport in and out of the sampled air

mass) and that the sink terms are constant over the time step considered.

The campaign time series of the steady-state NO$_3$ lifetime is presented in Fig. 5a. The night-to-night variability of τ_{ss}(NO$_3$) is very high throughout the 3 weeks of the campaign, with an average value of 200 s (± 100 s) for NO$_3$. The longest lifetimes (~ 1 h for NO$_3$) were observed during 3 consecutive nights on 30 and 31 August and 1 September.

In Fig. S3 in the Supplement, we plot the NO$_3$ steady-state lifetime, τ_{ss}(NO$_3$) and the lifetime calculated using the derivatives method, τ_{DER}(NO$_3$). Both calculations agree well for the lowest NO$_3$ lifetimes (first period of the campaign from 15 to 26 August). This is expected, as the steady-state condition is readily fulfilled when the losses of NO$_3$ (or N$_2$O$_5$) are rapid. During the nights 30 and 31 August and 1 September, τ_{ss}(NO$_3$) is up to 2 times greater than τ_{DER}(NO$_3$). This is clearly not related to the effects outlined above which apply to the first hours of darkness but, as we discuss later, is associated with deviation from steady state during these periods. The derivatives method does not provide data for the whole campaign. τ_{DER}(NO$_3$) is sometimes very scattered and sometimes negative, which arises from noise on the derivative terms. However, on average, the ratio τ_{ss}(NO$_3$) / τ_{DER}(NO$_3$) was 0.99 with ~ 66 % of the lifetimes agreeing within 30 %. The analysis and discussion below are based on the lifetimes obtained by the steady-state analysis.

The wind rose in Fig. 5b indicates that high values of τ_{ss}(NO$_3$) (≈ 1 h) were encountered irrespective of wind direction. This is initially surprising, as long NO$_3$ lifetimes values are not expected in air masses originating from the highly polluted sectors.

The short-term (hour-to-hour) variability was very high, as already described in Crowley et al. (2010) for this site. They describe the evolution of τ_{ss}(NO$_3$) over a single night in which the lifetime increased slowly after sunset to reach a roughly constant value around midnight. As steady state was predicted to be achieved on a much shorter timescale, and because other loss processes involving NO or heterogeneous loss of N$_2$O$_5$ were too slow, the increase in [NO$_3$] and τ_{ss}(NO$_3$) was interpreted as being due to a slow decrease in the concentration of VOCs, though measurements of VOCs were not available to confirm this. During the PARADE campaign a number of VOCs and the ASA were measured, allowing us to calculate the overall loss rate constant of NO$_3$ using Eq. (4). As only a subset of the suite of organic species likely to be present at the site was measured, this calculation will provide a lower limit for the overall NO$_3$ loss rate (and thus an upper limit for its real lifetime).

3.3.1 Loss of NO$_3$ via reaction with NO

With an average O$_3$ mixing ratio of about 40 ppbv, the NO lifetime at night is about 5 min, so that, in the absence of local sources and photochemical degradation of NO$_2$, the NO mixing ratio will be close to 0 within an hour of sunset. This
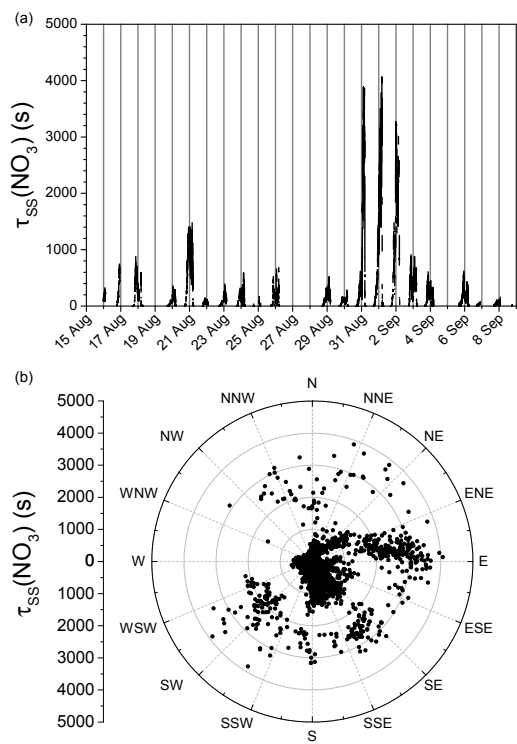
Figure 5. (a) τ_{ss}(NO$_3$) calculated according to Eq. (3). **(b)** τ_{ss}(NO$_3$) vs. wind direction.

Figure 6. (a) τ_{ss}(NO$_3$) and inverse loss rate constant (L_{NO})$^{-1}$, for loss of NO$_3$ via reaction with NO during the night of 23 August. Panels **(b)** and **(c)** display the associated [NO], [O$_3$], wind speed and wind direction data.

was the case for most of the nights during PARADE and NO measurements were below the (5 pptv) detection limit. On some nights, however, as exemplified in Fig. 6, 10–20 pptv of NO were measured, and between 21:00 UTC and sunrise τ_{ss}(NO$_3$) (Fig. 6a, black line) was consistent with that calculated from the NO reactivity as k_6[NO] (Fig. 6a, red line). During the period from 19:00 to 21:00 UTC the lifetime of NO$_3$ attributable to reaction with NO, τ(NO) is greater than τ_{ss}(NO$_3$), which may be due both to non-acquisition of steady state (for the first hour or so) and a contribution of other loss processes.

Figure 6 shows that the non-zero NO mixing ratios encountered on this night were in air masses associated with low wind speeds and may be a result of vehicle use on local roads or soil emissions.

3.3.2 Heterogeneous removal rate

The overall loss rate constant for NO$_3$ contains a contribution from indirect loss via the heterogeneous removal of N$_2$O$_5$ to particles as described by Eq. (4). In Fig. 7, we plot the calculated loss rate constant (s^{-1}) for NO$_3$ resulting from the uptake of N$_2$O$_5$ to particles (L_{HET} in blue) and compare it to the overall loss rate constant in steady state (L_{ss}, open circles) for two different nights. A simple temperature-dependent value of the uptake coefficient ($\gamma = 0.244$–$7.9 \times 10^{-4}T$) was used
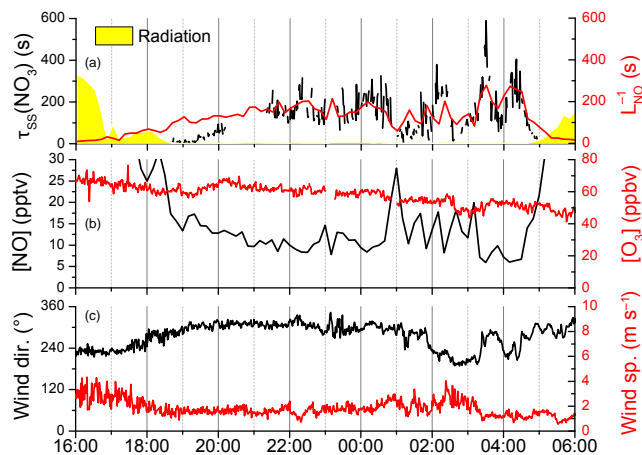
as recommended by IUPAC (Ammann et al., 2013). This expression is based on laboratory studies and results in a value at 283 K of $\sim 2 \times 10^{-2}$, which is larger than uptake coefficients obtained by analysis of both laboratory and field data in which the particle is not purely inorganic (Brown and Stutz, 2012). During periods when the NO$_3$ lifetime is long (e.g. τ_{ss}(NO$_3$) > 2000 s or L_{ss}(NO$_3$) $< 5 \times 10^{-4}$ s^{-1}) as on the second period of the night of the 30 August (Fig. 7b), when using the γ parameterisation above, the losses of N$_2$O$_5$ to particles can account entirely for the observed lifetimes or even exceed the steady-state reactivity, which may be the result of using a high value for γ. On this night, NO was below the instrumental detection limit and was not considered for NO$_3$ losses. During periods when the NO$_3$ lifetime is shorter (e.g. on 5 September, Fig. 7a) the indirect, heterogeneous loss represents only a small fraction of the overall loss. More sophisticated parameterisations of the uptake coefficient, including e.g. the nitrate and chloride content of the particles and the existence of organic coatings (Bertram and Thornton, 2009), often fail to reproduce in situ measurements (Bertram et al., 2009) and indicate that γ is a large source of uncertainty in these calculations. However, even the use of values as large as 0.1 does not reproduce the shorter lifetimes and, as previously discussed for this site (Crowley et al., 2010), the remaining losses are likely due to direct reactions of NO$_3$ with VOCs.

3.3.3 Loss of NO$_3$ via reaction with VOCs

The VOCs measured during PARADE are listed in Table 2 together with their rate constants (at 298 K) for reaction with NO$_3$. Among the trace gases listed, only a few of them (at high concentrations or with large rate constants for reaction with NO$_3$) contributed significantly to the loss of NO$_3$ and
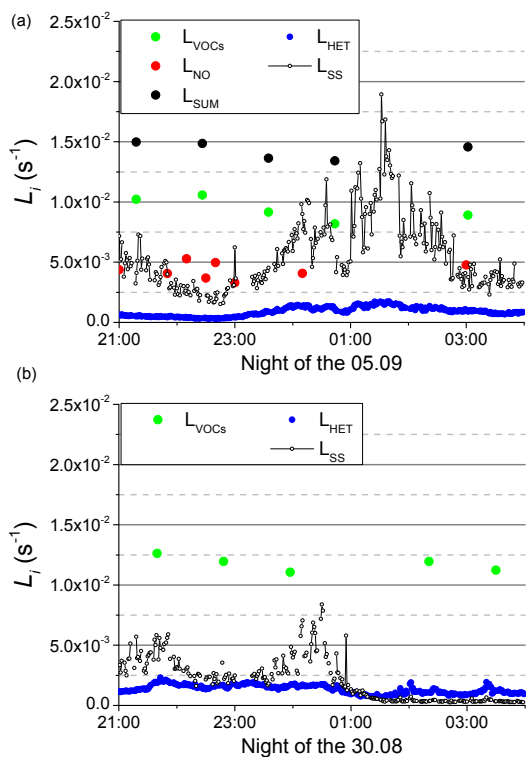
Figure 7. (a) Individual ($L_{\text{VOCs}} = \sum k_i [\text{VOC}]_i$, $L_{\text{NO}} = k_6 [\text{NO}]$ and L_{HET}) and summed NO$_3$ loss terms (L_{SUM}) for the night of 5 September, together with the loss rate constant of NO$_3$ in steady state (L_{ss}). **(b)** Individual ($L_{\text{VOCs}} = \sum k_i [\text{VOC}]_i$, $L_{\text{NO}} = k_6 [\text{NO}]$ and L_{HET}) and summed NO$_3$ loss terms (L_{SUM}) for the night of the 30 August, together with the inverse of the steady-state lifetime of NO$_3$ (L_{ss}). L_{VOCs}, L_{NO}, L_{HET} and L_{ss} are given in the original time resolutions (respectively 30, 10, 1 and 1 min). To calculate L_{SUM}, high-resolution L_{NO} and L_{HET} were interpolated to the L_{VOCs} time grid.

are highlighted in bold. Further discussion will focus on these VOCs. Apart from isoprene (up to 200 pptv), the mixing ratios of VOCs which are reactive towards NO$_3$ were generally below 100 pptv (see Supplement, Fig. S4). A clear diel cycle was observed for isoprene and during the warmer first and last parts of the campaign daytime mixing ratios were up to 5 times higher than during the night. For the monoterpenes the diel cycle was less pronounced and on two nights (4–5 September and 5–6 September) large mixing ratios were observed during the night (e.g. > 50 pptv for myrcene and limonene), which were not accompanied by increases in isoprene. As expected, during colder, rainy periods, the BVOCs were less abundant and showed a weaker diel variation.

For each monoterpene, the NO$_3$ loss rate constant for reaction with VOCs ($L_i = k_i [\text{VOC}]_i$ where k_i is the rate constant for each VOC) is plotted together with the steady-state NO$_3$ total reactivity ($L_{\text{ss}}(\text{NO}_3)$) and the VOCs summed reactivities (including alkanes and alkenes) in Figs. 7 and S5. The rate coefficients for reaction of NO$_3$ with the VOCs were de-

rived from the temperature-dependent expressions given by IUPAC and were calculated at each time step of the data set. Figure S5 shows that, over almost the whole campaign, the steady-state loss rate constants L_{ss} (open circles) are significantly lower than those calculated by summing the individual contributions of the VOCs (L_{VOCs}, dashed line). Indeed, during the 3 nights in which very long NO$_3$ lifetimes were encountered, L_{ss} is approximately 4 to 5 times lower than that expected from the summed VOCs. In other words, within the steady-state framework used here and using the NO$_3$ production term, $k_1 [\text{NO}_2][\text{O}_3]$, the observed mixing ratios and lifetimes of NO$_3$ are incompatible with the VOC measurements.

The divergence between the steady-state loss rates and that obtained by summing the losses with each VOC is exacerbated when one considers that the VOCs measured in PARADE cover only a fraction of those present in the air so that L_{VOCs} must strictly be regarded as a lower limit. As exemplified in Figs. 7 and S5, summing the individual loss rate constants due to reaction of NO$_3$ with NO (L_{NO}), the complete set of VOCs (L_{VOCs}) and indirect loss via heterogeneous uptake of N$_2$O$_5$ to available particles (L_{HET}) results in an air-mass reactivity that is larger than that derived from the steady-state calculations, i.e. the NO$_3$ lifetime is longer than expected (or its concentration higher). Generally, the opposite is observed and missing reactivity is assigned e.g. to VOCs that were not measured. Below, we examine possible explanations for this, including the breakdown of the steady-state assumption, the potential role of other chemical routes to NO$_3$ generation and meteorological effects.

3.3.4 NO$_3$ production rate

So far, our calculations have been based on the assumption that NO$_3$ is generated solely in the reaction between NO$_2$ and O$_3$ (Reaction R1, see Sect. 3.3). If NO$_3$ is only formed via Reaction (R1), the uncertainty associated with $P(\text{NO}_3)$, propagated from those of [NO$_2$] and [O$_3$] is approximately 8 %. The good agreement between several devices for measurement of both NO$_2$ and O$_3$ indicates that the term $k_1 [\text{NO}_2][\text{O}_3]$ is indeed well defined. As indicated in Sect. 1, other sources of NO$_3$ are known but are generally regarded as negligible. The reaction of OH with HNO$_3$ (Reaction R2) generates NO$_3$ at $\sim$ 100 % yield but, even assuming nighttime concentrations of hydroxyl radicals of 1×10^5 molecule cm^3 and 2 ppbv of HNO$_3$, the NO$_3$ production rate is only $\sim$ 1 % of that from Reaction (R1). In the absence of sunlight, the formation of NO$_3$ from the photolysis (Reaction R3) of halogen nitrate, XONO$_2$ (where X = Cl, Br or I), will not contribute at nighttime. A further possible source of nighttime NO$_3$ and cause for error in steady-state lifetime estimations could be the rapid recycling of NO$_3$ from the products formed in its initial reaction with BVOCs, as has been seen for the OH radical (Lelieveld et al., 2008; Taraborrelli et al., 2012). The organic nitrates formed as first-generation products when NO$_3$ reacts with biogenic VOCs

Table 2. VOCs measured using GC-MS and GC-FID during PARADE.

GC-MS VOCs	$k(NO_3 + VOC)^a$	Maximum mixing ratio (pptv)	GC-FID VOCs	$k(NO_3 + VOC)^a$	Maximum mixing ratio (ppbv)
Isoprene	7.0×10^{-13}	220	Ethane	$< 1 \times 10^{-17}$	7.2
α-Pinene	6.2×10^{-12}	170	Ethene	2.1×10^{-16}	15
Myrcene	1.1×10^{-11}	70	Propane	$< 7 \times 10^{-17}$	2.5
Limonene	1.22×10^{-11}	130	Propene	9.5×10^{-15}	20
p-Cymene	$1.0 \times 10^{-15\ b}$	20	i-Butane	$1.1 \times 10^{-16\ b}$	1.3
Benzene	$< 3 \times 10^{-17\ b}$	230	n-Butane	4.6×10^{-17}	1.4
Toluene	$7.0 \times 10^{-17\ b}$	420	cis-2-Butene	3.5×10^{-13}	0.6
Ethylbenzene	$< 6 \times 10^{-16\ b}$	80	i-Pentane	$1.62 \times 10^{-16\ b}$	1
m-Xylene	$2.6 \times 10^{-16\ b}$	130	n-Pentane	$8.7 \times 10^{-17\ b}$	1
p-Xylene	$5.0 \times 10^{-16\ b}$	65	1-Pentene	$1.5 \times 10^{-14\ b}$	1.9
o-Xylene	$4.1 \times 10^{-16\ b}$	75	Butadiene	$1.0 \times 10^{-13\ b}$	10.6

[a] Rate constants (cm^3 molecule^{-1} s^{-1}) at 298 K taken from the latest evaluation (Atkinson et al., 2006; Ammann et al., 2016) unless noted otherwise.
[b] Rate constants (cm^3 molecule^{-1} s^{-1}) taken from Atkinson and Arey (2003).

are, however, believed to be chemically stable and there is no obvious pathway for rapid re-release of NO$_3$ once formed.

We now consider a further nighttime process forming NO$_3$ via the oxidation of NO$_2$ by stabilised Criegee intermediates (sCIs), which are formed in the atmosphere by the reaction of O$_3$ with biogenic and anthropogenic alkenes (Johnson and Marston, 2008). This may be especially relevant when observing apparently long NO$_3$ lifetimes (i.e. high concentrations) in the presence of reactive VOCs.

The possibility of NO$_3$ generation via sCI reaction with NO$_2$ was first raised several years ago (Fenske et al., 2000; Presto and Donahue, 2004), though in the early studies, which were unable to detect Criegee radicals directly, uncertainties regarding the products and the rate constant were large. In recent work (Welz et al., 2012) on the reaction between the simplest sCI (CH$_2$O$_2$) and NO$_2$, a large rate constant ($7^{+3}_{-2}10^{-12}$ cm^3 molecule^{-1} s^{-1}) was determined. The authors hypothesised that the reaction between other sCI and NO$_2$ might have similar rate constants. A further study (Stone et al., 2014) reports a rate constant ($1.5 \pm 0.5 \times 10^{-12}$ cm^3 molecule^{-1} s^{-1}) for the same reaction and detected HCHO as product, consistent with an O-atom transfer from sCI to NO$_2$ to form NO$_3$. Subsequently, the formation of NO$_3$ (and N$_2$O$_5$) resulting from the photolysis at 248 nm of a mixture of CH$_2$I$_2$, O$_2$ and NO$_2$ was attributed to the reaction between CH$_2$O$_2$ and NO$_2$ (Ouyang et al., 2013). Whether sCI can contribute significantly to nighttime NO$_3$ formation or not depends on the assumption that all sCIs react with a similar rate coefficient to CH$_2$O$_2$, that NO$_3$ is formed at high yield and that sufficient sCIs are present in the nighttime boundary layer. In Table 3, we assess the three reactions that could have contributed to NO$_3$ formation during PARADE. We take a generic rate coefficient for sCI + NO$_2$ that lies between the literature determinations (Welz et al.,

2012; Stone et al., 2014) and assume 100 % product yield for formation of NO$_3$.

Table 3 shows that, whereas the reaction between OH and HNO$_3$ can safely be neglected, the reaction between sCI and NO$_2$ can represent a significant fraction of the total rate of production of NO$_3$ if sCIs are present at ~ 0.1 pptv during night. This reflects the fact that, although Criegee radicals are expected to be present at concentrations 4–6 orders of magnitude less than those of O$_3$, the rate constant for reaction with NO$_2$ is ~ 5 orders of magnitude larger.

The rate of formation of sCIs in the boundary layer depends on both the concentration and nature of the organics reacting with O$_3$ to form it and is expected to be very variable. Likewise, the sink reactions of sCIs are difficult to predict, though reactions with water vapour, SO$_2$ and NO$_2$ are expected to be important (Vereecken et al., 2012). Boundary-layer mixing ratios of sCIs are thus associated with great uncertainty. Based on a steady-state approach, sCI mixing ratio up to 0.03 pptv have ben calculated for the PARADE campaign (Bonn et al., 2014), i.e. within the range of values used in Table 3. Recent measurements in a Boreal forest environment estimated sCI mixing ratios to be 0.0025 to 0.04 pptv (Taipale et al., 2014) and sCIs have been tentatively identified (Mao et al., 2012) as the source of an interfering signal in ambient measurements of OH that may approach 0.2 pptv (Novelli et al., 2014). As not all ambient sCIs will decompose to OH within such instruments, the wider implication is that pptv amounts of sCI may be present.

To calculate the influence of sCI-induced formation of NO$_3$ during the PARADE campaign we recalculated the NO$_3$ production rate assuming two different sCI concentrations at the limits of the range listed in Table 3 and using the rate constant given. In Fig. 8 we display the calculated steady-state lifetime without sCI reactions forming NO$_3$ (black symbols) and the effect of using a low sCI concentration (τ_{LsCI}, blue

Table 3. Reactions producing NO$_3$.

Reaction	Mixing ratio first reactant	Mixing ratio second reactant	Rate coefficient (298 K)[a]	$P(NO_3)$[b]
$O_3 + NO_2$	20–50 ppbv	0.5–5 ppbv	3.5×10^{-17}	$(0.9–220) \times 10^{-3}$
$OH + HNO_3$	$(1–10) \times 10^{-2}$ pptv	0.5–5 ppbv	1.5×10^{-13}	$(1.9–190) \times 10^{-5}$
$sCI + NO_2$	0.01–0.1 pptv	0.5–5 ppbv	5.0×10^{-12}	$(0.6–6) \times 10^{-3}$

[a] Units of cm^3 molecule^{-1} s^{-1}. [b] Units of pptv s^{-1}.
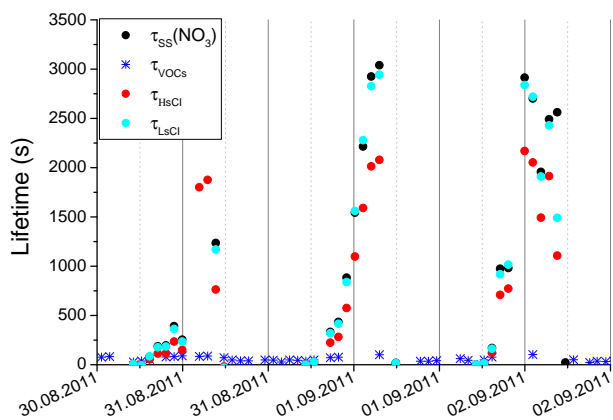
Figure 8. NO$_3$ steady-state lifetimes calculated using different production terms. Black data points: only NO$_2$+O$_3$ forms NO$_3$. Blue circles: additional formation from 0.01 pptv sCI reacting with NO$_2$. Red data points: additional formation from 0.1 pptv sCI reacting with NO$_2$. The inverse of L_{VOCs} is indicated by the blue stars. Similar to Fig. 7, all data were interpolated to the VOC time axis; hence the low time resolution.

symbols) or a high concentration (τ_{HsCI}, red symbols). The resultant reduction in the calculated steady-state lifetime of NO$_3$ is significant when using the higher values of [sCI]. For example, on 31 August, the largest value of $\tau_{ss}(NO_3)$ would be reduced from 3000 s (black data points) to 2000 s (red data points) when assuming 0.1 pptv of sCI. However, in order to bring the steady-state lifetime into agreement with that based on the VOC measurements (green symbols), a sCI mixing ratio of 4 pptv would be required. Our present knowledge of Criegee formation and loss mechanisms under atmospheric conditions precludes accurate assessment of their role in forming NO$_3$ at nighttime, though sCI mixing ratios as large as 4 pptv appear (at present) unlikely, though not impossible.

3.3.5 Meteorological considerations

We have shown that, while uncertainties in some parameters required for calculation of NO$_3$ lifetimes exist, they are likely to be insufficient to explain the high concentrations (and lifetimes) of NO$_3$ during the nights of 30 August to 1 September.

Close examination of the NO$_3$ lifetime on these nights (e.g. Fig. 9) reveals an especially strong gradient, with $\tau_{ss}(NO_3)$ values increasing e.g. by 500 to 600 % over the course of an hour. Simultaneously, $\tau_{ss}(N_2O_5)$ values (not shown) increase by 200 %. The smaller increase in $\tau_{ss}(N_2O_5)$ is due to a simultaneous decrease of [NO$_2$] by 50 %, thus shifting the equilibrium towards NO$_3$. The large gradient in $\tau_{ss}(NO_3)$ cannot be attributed to a decrease in the mixing ratios of reactive trace gases, which were much less variable (see above). We therefore consider the possibility that the long lifetimes observed on these nights are related to sampling air masses from a low-lying residual layer (i.e. from above a particulary shallow nocturnal boundary layer) which, especially at low wind speeds, is decoupled from ground emissions of NO$_x$ and VOCs, allowing NO$_3$ and N$_2$O$_5$ to build up to higher levels and would also help to explain the lack of dependence on wind direction.

The hypothesis that sampling of residual-layer air is responsible for the long steady-state lifetimes of NO$_3$ and their apparent incompatibility with the VOC measurements is examined in detail in Fig. 9. Here, the time profiles of $\tau_{ss}(NO_3)$, NO$_2$, O$_3$, CO$_2$, and ASA and some meteorological parameters are plotted for the night of 30 August. The night from 30 to 31 August can be divided into two distinct periods. Between 21:00 and 00:30 UTC (first period) $\tau_{ss}(NO_3)$ was roughly constant at an average value of about 150 s. After this, we observed a large increase in the NO$_3$ steady-state lifetime between $\sim$ 00:30 and 01:30 UTC, followed by period 2 (01:30 UTC until dawn) in which $\tau_{ss}(NO_3)$ was consistently close to 3000 s.

The transition from the shorter (period 1) to longer (period 2) lifetimes is accompanied by a decrease in the NO$_2$ mixing ratio from about 2.5 to 1 ppbv, a $\sim$ 2 ppmv decrease in CO$_2$, an increase in O$_3$ from $\sim$ 15 to 25 ppbv and a $\sim$ 30 % increase in particle surface area. Changes in the local wind direction (at $\sim$ 20 m height) between the clean northern sector to the anthropogenically polluted south sector during this second period did not impact the NO$_x$ levels or the NO$_3$ lifetime.

These observations are consistent with air from the residual layer being sampled during the second period. Higher levels of O$_3$ and particles, formed during the previous day in the turbulently mixed boundary layer, are expected in the residual layer compared to the shallow, nocturnal boundary
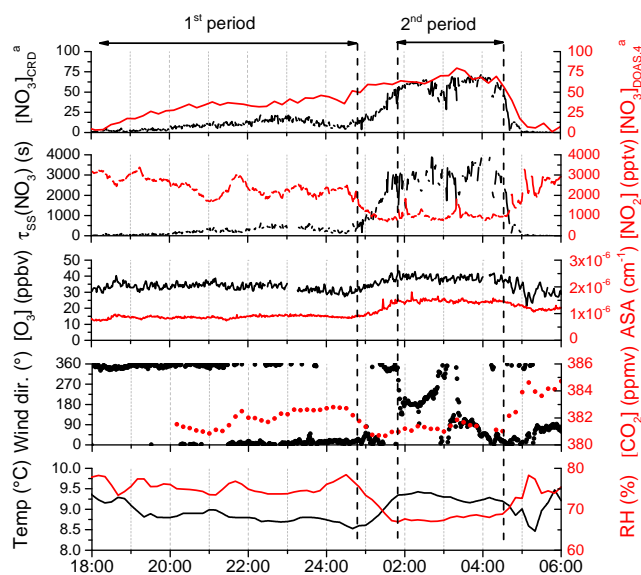
Figure 9. Detailed view of the night of the 30 August indicating two periods corresponding to different NO$_3$ lifetime regimes. The trends in NO$_3$ lifetime, CO$_2$, NO$_2$, O$_3$, RH and aerosol surface area (ASA) indicate a transition from boundary-layer to residual-layer air between $\sim$ 00:30 and 01:30 UTC in the morning. Sunrise was at about 05:00 UTC. [a] Units of pptv.

layer in which dry deposition is important for both. Conversely, levels of NO$_2$, formed from oxidation of ground-level NO emissions are expected to be higher in the lower levels (Stutz et al., 2004; Brown et al., 2007) and thus decrease when sampling air from the residual layer. The second period is also marked by a significant drop in relative humidity (from $\sim$ 80 to 65 %) and an increase in the temperature of $\approx$ 1 °C. The former is expected as relative humidity decreases above the nocturnal boundary layer. A correlation between increasing NO$_3$ lifetimes and temperature has been observed previously (Crowley et al. 2010) and was attributed to downward movement of higher air masses during an inversion.

Figure 10a and b show profiles of the potential temperature and relative humidity within the first period at 19:00 UTC and within the second period at 04:00 UTC from 30 to 31 August. The temporal development of the temperature and the relative humidity profiles agrees well with the near-surface observations. The profiles of the potential temperature show a change from stable stratification (potential temperature increase with height) to neutral stratification (potential temperature is constant with height) which is an additional indication that the measurements within period 2 were obtained within the residual layer. The same temporal development of the potential temperature profiles was observed 24 h later (Fig. 10a, b), when again the NO$_3$ lifetime was enhanced. On both nights, the lack of a switch in sign of the RH gradient with height at 04:00 UTC contrasts with the profiles at 19:00 and 06:00 UTC which show clear evidence for a switch from
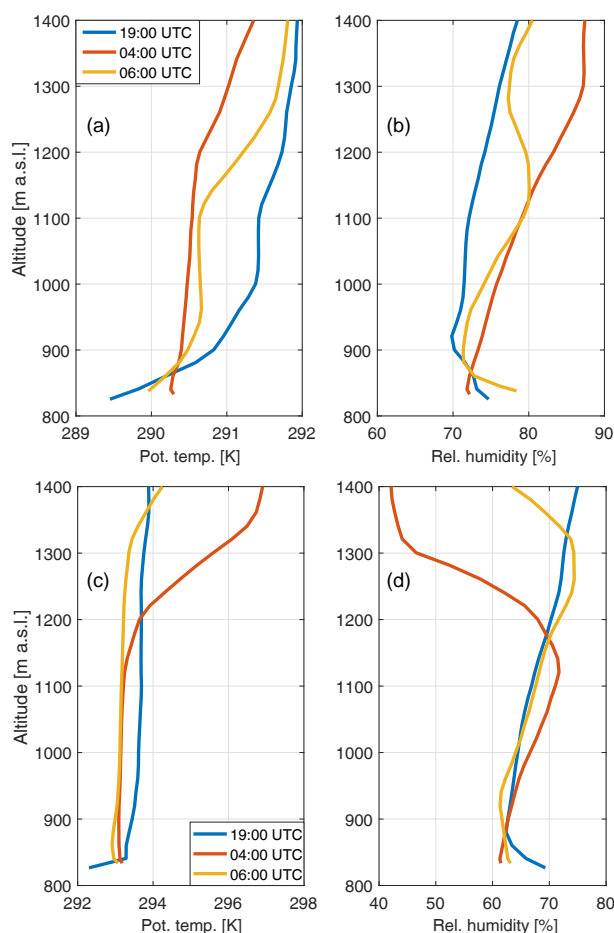

Figure 10. Vertical profiles of the potential temperature **(a)** and the relative humidity **(b)** during the first period on 30 August at 19:00 UTC (blue), as shown in Fig. 9, and on 31 August at 04:00 UTC (red) and 06:00 UTC (orange, after sunrise) during the second period. **(c, d)** Same as above but for 31 August to 1 September.

boundary layer to residual layer some 50 to 100 m above the summit. Between 31 August and 2 September we observed no nocturnal build-up of CO$_2$, which strongly contrasts the periods prior to and after this period (see Fig. S6) and again indicates that this period with the longest NO$_3$ lifetimes is associated with residual-layer air.

When sampling from the residual layer, we would expect that the observed increase in O$_3$ and ASA and simultaneous decrease in NO$_2$ and RH would be accompanied by a decrease in those biogenic trace gases, which are reactive towards NO$_3$. Indeed, if we take the measured NO$_3$ mixing ratio of 200 pptv on 2 September, we calculate that the lifetime of biogenics such as limonene should be of the order of only a few minutes in the residual layer. The simultaneous measurement of both high NO$_3$ steady-state lifetimes and terpene mixing ratios can now be explained if we consider that the terpene emissions are only local, i.e. from trees that are close

to the top of the mountain (and our inlet) and thus also within the residual layer. Such local emission (e.g. within 30 m of the inlet) does not allow the NO$_3$+ terpene chemistry to go to steady state so that only a fraction of the NO$_3$ (and terpene) are consumed. The extent of reaction will be related to the location of the emission relative to the inlet and local wind speeds and is likely to be highly variable.

So far, we have assumed that NO$_3$ (or N$_2$O$_5$) levels aloft (i.e. in the residual layer) are enhanced w.r.t. the boundary layer. As NO$_3$ (and also NO$_2$ and O$_3$) was measured by LP-DOAS at different heights, this data set should give some insight into the occurrence and extent of vertical gradients in NO$_3$ concentrations. In Fig. 9 we plot a data set obtained using the LP-DOAS. In the first period (until ∼ 00:30 UTC), the DOAS measurements of NO$_3$ at the highest altitude were significantly larger (factor of ∼ 5 at 24:00 UTC) than those measured by the CRDS. This difference in concentration disappeared during the second phase (01:30 until 04:00 UTC) when both instruments measured high NO$_3$, thus supporting the concept that the top of the mountain is in the residual layer during this period. Below, we compare the CRDS and DOAS measurements in more detail.

3.3.6 Comparison of NO$_3$ lifetimes derived from CRDS and LP-DOAS instruments

As mentioned in Sect. 2.2 the LP-DOAS measurements were conducted using a total of four light paths. For this analysis we compare data retrieved from only the lowest (835 to 872 m a.s.l.) and highest (835 to 959 m a.s.l.) levels (see Fig. 11). By comparison, the height of the CRDS inlet was ∼ 838 m a.s.l.

We refer to the lower and higher levels as DOAS 1 and DOAS 4 respectively. Steady-state NO$_3$ lifetimes were calculated in the same way as described above for the CRDS data set, using the NO$_2$ and O$_3$ data obtained from the DOAS instrument at those two different levels. Because of the short horizontal (1.5 km) and vertical (∼ 125 m) range of the DOAS light paths, the integrated temperature over both light paths is assumed to be the same as the temperature measured at the Kleiner Feldberg hilltop and these values were used to calculate the rate constant (k_1) for NO$_3$ production. Note that differences in temperature of a few Kelvin do not impact significantly the rate constant, k_1.

In Fig. 12 we plot the NO$_3$ mixing ratios and steady-state lifetimes obtained on two different nights, 1–2 and 5–6 September, by the CRDS and LP-DOAS instruments. While the night of 5–6 September shows large differences between the mixing ratios reported by the CRDS and LP-DOAS instruments, and a strong vertical gradient in NO$_3$, good agreement, i.e. a weak (or 0) gradient, is observed on 1–2 September. The LP-DOAS measurements of the NO$_2$ (Thieser et al., 2016) and O$_3$ mixing ratios (Fig. 13) reveal little or no difference between the highest and lowest light paths over the whole campaign, so that the NO$_3$ production term
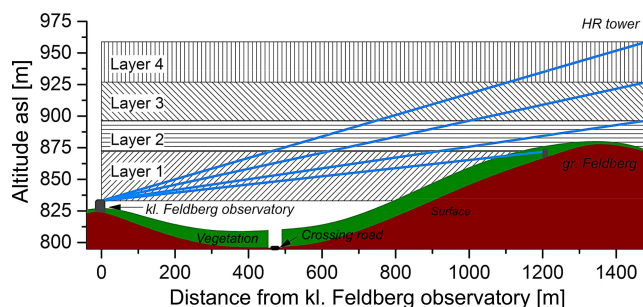

Figure 11. Schematic diagram of the LP-DOAS light paths deployed during the PARADE campaign, with the Kleiner Feldberg on the left and the Grosser Feldberg on the right. The LP-DOAS data sets used in this work are those obtained from the lower-most and upper-most light paths.
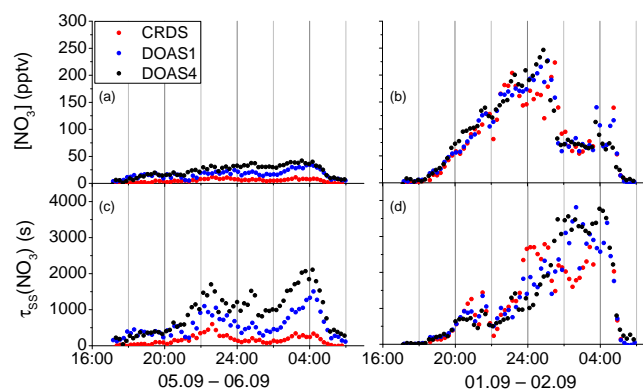

Figure 12. [NO$_3$] **(a)** and τ_{ss}(NO$_3$) **(c)** using CRDS data (red), lowest LP-DOAS light path (DOAS 1) and highest LP-DOAS light path (DOAS 4) for the night of 5–6 September. **(b, d)** As for the left-hand plot but showing data for the night of 1–2 September.

was roughly constant with altitude. The clear dependence of the NO$_3$ mixing ratio on height on 5–6 September is thus due to variation in the NO$_3$ loss term. Figure 12c indicates a factor of up to ∼ 5 increase in NO$_3$ lifetime when comparing the LP-DOAS data at the highest level to the CRDS measurements.

In Fig. 14a we plot the campaign NO$_3$ mixing ratios measured by the CRDS and DOAS 4 vs. the DOAS 1 data set. As mentioned previously and illustrated in Fig. 11, the LP-DOAS light source and the CRDS inlet were co-located at a height of ∼ 835 m whilst the LP-DOAS retroreflectors were at ∼ 959 and 872 m. All data which were above the detection limit (10 pptv for LP-DOAS and 5 pptv for the CRDS) were included. The coloured lines (black, blue and red) represent slopes of 0.5, 1 and 2 respectively. Nearly all of the black data points [NO$_3$]$_{DOAS4}$ have slopes between 1 and 2, indicating that, on average, [NO$_3$] is higher aloft, consistent with previous observations of positive vertical gradients in NO$_3$ (Stutz et al., 2004; Brown et al., 2007). At large mixing ratios, i.e. for [NO$_3$]$_{DOAS1}$ > 100 pptv, the al-
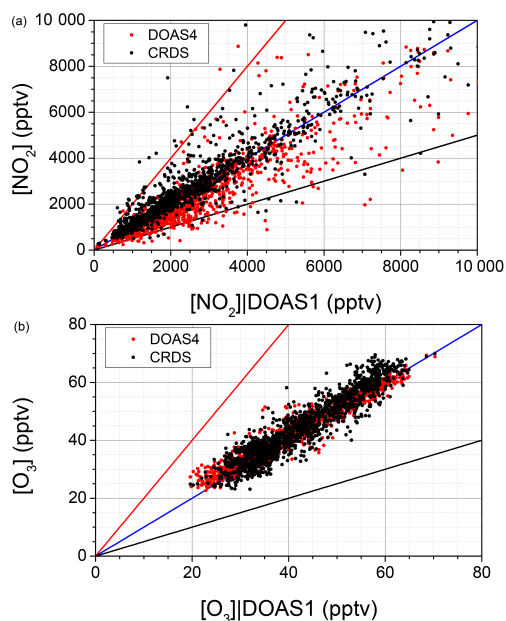
Figure 13. (a) Comparison between $[NO_2]_{CRDS}$, $[NO_2]_{DOAS4}$ and $[NO_2]_{DOAS1}$ (whole campaign). **(b)** Comparison between $[O_3]_{CRDS}$, $[O_3]_{DOAS4}$ and $[O_3]_{DOAS1}$ (whole campaign). Blue lines have a gradient of 1, red lines a gradient of 2 and black lines a gradient of 0.5.

Figure 14. (a) $[NO_3]_{CRDS}$ (red) and $[NO_3]_{DOAS4}$ (black) vs. $[NO_3]_{DOAS1}$. **(b)** $\tau_{ss}(NO_3)_{CRDS}$ (red) and $\tau_{ss}(NO_3)_{DOAS4}$ (black) vs. $\tau_{ss}(NO_3)_{DOAS1}$. Coloured lines on both panels represent slopes of 0.5, 1 and 2 (black, blue and red respectively).

titude dependence on the $[NO_3]$ is weaker and the black points are closer to the blue line (slope of 1). The ratio between $[NO_3]_{CRDS}$ and $[NO_3]_{DOAS1}$ also shows some dependence on the NO$_3$ mixing ratio. When the NO$_3$ mixing ratios are low, the ratio CRDS / LP-DOAS is also low and generally less than 0.5. In extreme cases, the $[NO_3]_{CRDS}$ values are close to a few pptv or below the detection limit while $[NO_3]_{DOAS1}$ measured as high as 40 to 50 pptv. To illustrate this, for NO$_3$ steady-state lifetimes of < 1500 (i.e. all nights except for 30 August–2 September) the average value of the $[NO_3]_{DOAS4} / [NO_3]_{DOAS1}$ ratio is 1.23 ± 0.07, whereas for NO$_3$ steady-state lifetimes of > 1500 s we derive a $[NO_3]_{DOAS4} / [NO_3]_{DOAS1}$ ratio of 0.95 ± 0.05.

Both $\tau_{ss}(NO_3)_{CRDS}$ and $\tau_{ss}(NO_3)_{DOAS4}$ data sets (Fig. 14b) show the same trends as the one described for $[NO_3]$. At low $\tau_{ss}(NO_3)_{DOAS1}$ the black and red points are respectively closer to the black and red lines and as $\tau_{ss}(NO_3)_{DOAS1}$ increases to the highest values the data points are all closer to the blue line. The apparent dependence of the NO$_3$ mixing ratios and lifetime on the NO$_3$ concentrations reflects the fact that, when NO$_3$ is high, both instruments are sampling the residual layer in which NO$_3$ levels are expected to be higher and gradients in NO$_3$ are expected to be weaker than found close to the surface (Brown et al., 2007).

In summary, the data shown in Fig. 9 and the LP-DOAS measurements of NO$_3$ at different altitudes provide compelling evidence for a low-lying residual layer (or very shallow nocturnal boundary layer) being responsible for the oc-
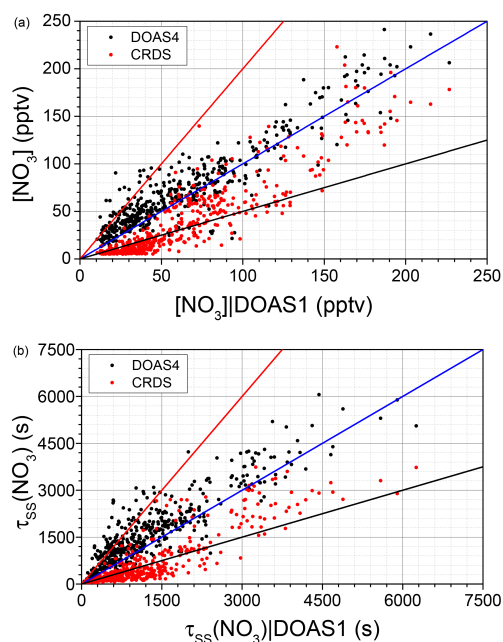
casional observation of high NO$_3$ mixing ratios seen by the ground-level CRDS instrument and the associated long steady-state lifetimes. This layer will be most stable and thus best decoupled from the underlying boundary layer when wind speeds are low. The DOAS measurement of concentration at different altitudes does not contain information about the vertical exchange and mixing itself. Any estimation of vertical mixing for a reactive trace gas like NO$_3$ would require a chemical model with transport, which would be difficult for such an environment with complex topography like the Kleiner Feldberg.

4 Conclusions

We observed highly variable NO$_3$ concentrations and lifetimes at a mountain site in south-west Germany. Measurements of NO$_3$, its precursors and its sink reactions (both direct and indirect) enabled assessment of the processes (both chemical and meteorological) influencing its steady-state lifetime. We found that, during several nights, the observed steady-state lifetime was frequently larger than expected based on measured gas-phase reactants such as VOCs and NO. We have shown that an enhancement in the NO$_3$ production term via the reaction between Criegee and NO$_2$ may be significant but unlikely to explain the discrepancy. The periods with the highest apparent NO$_3$ lifetimes were associated with the presence of a very shallow boundary layer at the mountaintop so that the instrument inlets sampled from

the residual layer and NO$_3$ (and N$_2$O$_5$) mixing ratios and lifetimes were larger than those calculated from measured sources and sink terms.

Data availability

The PARADE data can be obtained on request (via John Crowley) from the owners.

The Supplement related to this article is available online at doi:10.5194/acp-16-4867-2016-supplement.

References

Allan, B. J., Carslaw, N., Coe, H., Burgess, R. A., and Plane, J. M. C.: Observations of the nitrate radical in the marine boundary layer, J. Atmos. Chem., 33, 129–154, 1999.

Ammann, M., Cox, R. A., Crowley, J. N., Jenkin, M. E., Mellouki, A., Rossi, M. J., Troe, J., and Wallington, T. J.: Evaluated kinetic and photochemical data for atmospheric chemistry: Volume VI – heterogeneous reactions with liquid substrates, Atmos. Chem. Phys., 13, 8045–8228, doi:10.5194/acp-13-8045-2013, 2013.

Ammann, M., Cox, R. A., Crowley, J. N., Jenkin, M. E., Mellouki, A., Rossi, M. J., Troe, J., and Wallington, T. J.: IUPAC: Task Group on Atmospheric Chemical Kinetic Data Evaluation, available at: http://iupac.pole-ether.fr/index.html, last access: February 2016.

Asaf, D., Pedersen, D., Matveev, V., Peleg, M., Kern, C., Zingler, J., Platt, U., and Luria, M.: Long-term measurements of NO$_3$ radical at a semiarid, urban Site: 1. Extreme concentration events and their oxidation capacity, Environ. Sci. Technol., 43, 9117–9123, doi:10.1021/es900798b, 2009.

Atkinson, R. and Arey, J.: Atmospheric degradation of volatile organic compounds, Chem. Rev., 103, 4605–4638, doi:10.1021/cr0206420, 2003.

Atkinson, R., Baulch, D. L., Cox, R. A., Crowley, J. N., Hampson, R. F., Hynes, R. G., Jenkin, M. E., Rossi, M. J., and Troe, J.: Evaluated kinetic and photochemical data for atmospheric chemistry: Volume I – gas phase reactions of O$_x$, HO$_x$, NO$_x$ and SO$_x$ species, Atmos. Chem. Phys., 4, 1461–1738, doi:10.5194/acp-4-1461-2004, 2004.

Atkinson, R., Baulch, D. L., Cox, R. A., Crowley, J. N., Hampson, R. F., Hynes, R. G., Jenkin, M. E., Rossi, M. J., Troe, J., and IUPAC Subcommittee: Evaluated kinetic and photochemical data for atmospheric chemistry: Volume II – gas phase reactions of organic species, Atmos. Chem. Phys., 6, 3625–4055, doi:10.5194/acp-6-3625-2006, 2006.

Behnke, W., George, C., Scheer, V., and Zetzsch, C.: Production and decay of ClNO$_2$ from the reaction of gaseous N$_2$O$_5$ with NaCl solution: Bulk and aerosol experiments, J. Geophys. Res., 102, 3795–3804, 1997.

Berkes, F., Hoor, P., Bozem, H., Kunkel, D., Sprenger, M., and Henne, S.: Airborne observation of mixing across the entrainment zone during PARADE 2011, Atmos. Chem. Phys. Discuss., 15, 29171–29212, doi:10.5194/acpd-15-29171-2015, 2015.

Bertram, T. H. and Thornton, J. A.: Toward a general parameterization of N$_2$O$_5$ reactivity on aqueous particles: the competing effects of particle liquid water, nitrate and chloride, Atmos. Chem. Phys., 9, 8351–8363, doi:10.5194/acp-9-8351-2009, 2009.

Bertram, T. H., Thornton, J. A., Riedel, T. P., Middlebrook, A. M., Bahreini, R., Bates, T. S., Quinn, P. K., and Coffman, D. J.: Direct observations of N$_2$O$_5$ reactivity on ambient aerosol particles, Geophys. Res. Lett., 36, L19803, doi:10.1029/2009GL040248, 2009.

Bonn, B., Bourtsoukidis, E., Sun, T. S., Bingemer, H., Rondo, L., Javed, U., Li, J., Axinte, R., Li, X., Brauers, T., Sonderfeld, H., Koppmann, R., Sogachev, A., Jacobi, S., and Spracklen, D. V.: The link between atmospheric radicals and newly formed particles at a spruce forest site in Germany, Atmos. Chem. Phys., 14, 10823–10843, doi:10.5194/acp-14-10823-2014, 2014.

Brown, S. S. and Stutz, J.: Nighttime radical observations and chemistry, Chem. Soc. Rev., 41, 6405–6447, 2012.

Brown, S. S., Stark, H., and Ravishankara, A. R.: Applicability of the steady state approximation to the interpretation of atmospheric observations of NO$_3$ and N$_2$O$_5$, J. Geophys. Res.-Atmos., 108, 4539, doi:10.1029/2003JD003407, 2003.

Brown, S. S., Dubé, W. P., Osthoff, H. D., Wolfe, D. E., Angevine, W. M., and Ravishankara, A. R.: High resolution vertical distributions of NO$_3$ and N$_2$O$_5$ through the nocturnal boundary layer, Atmos. Chem. Phys., 7, 139–149, doi:10.5194/acp-7-139-2007, 2007.

Brown, S. S., deGouw, J. A., Warneke, C., Ryerson, T. B., Dubé, W. P., Atlas, E., Weber, R. J., Peltier, R. E., Neuman, J. A., Roberts, J. M., Swanson, A., Flocke, F., McKeen, S. A., Brioude, J., Sommariva, R., Trainer, M., Fehsenfeld, F. C., and Ravishankara, A. R.: Nocturnal isoprene oxidation over the Northeast United States in summer and its impact on reactive nitrogen partitioning and secondary organic aerosol, Atmos. Chem. Phys., 9, 3027–3042, doi:10.5194/acp-9-3027-2009, 2009.

Brown, S. S., Dube, W. P., Peischl, J., Ryerson, T. B., Atlas, E., Warneke, C., de Gouw, J. A., Hekkert, S. t. L., Brock, C. A., Flocke, F., Trainer, M., Parrish, D. D., Feshenfeld, F. C., and Ravishankara, A. R.: Budgets for nocturnal VOC oxidation by nitrate radicals aloft during the 2006 Texas Air Quality Study, J. Geophys. Res.-Atmos., 116, D24305, doi:10.1029/2011jd016544, 2011.

Crowley, J. N., Schuster, G., Pouvesle, N., Parchatka, U., Fischer, H., Bonn, B., Bingemer, H., and Lelieveld, J.: Nocturnal nitrogen oxides at a rural mountain-site in south-western Germany, Atmos. Chem. Phys., 10, 2795–2812, doi:10.5194/acp-10-2795-2010, 2010.

Crowley, J. N., Thieser, J., Tang, M. J., Schuster, G., Bozem, H., Beygi, Z. H., Fischer, H., Diesch, J.-M., Drewnick, F., Borrmann, S., Song, W., Yassaa, N., Williams, J., Pöhler, D., Platt, U., and Lelieveld, J.: Variable lifetimes and loss mechanisms for NO$_3$ and N$_2$O$_5$ during the DOMINO campaign: contrasts between marine, urban and continental air, Atmos. Chem. Phys., 11, 10853–10870, doi:10.5194/acp-11-10853-2011, 2011.

Draxler, R. R. and Rolph, G. D.: HYSPLIT (HYbrid Single-Particle Lagrangian Integrated Trajectory) Model access via NOAA ARL READY Website, NOAA Air Resources Laboratory, Silver Spring, MD, USA, available at: http://ready.arl.noaa.gov/HYSPLIT.php (last access: January 2012), 2011.

Drewnick, F., Böttger, T., von der Weiden-Reinmüller, S.-L., Zorn, S. R., Klimach, T., Schneider, J., and Borrmann, S.: Design of a mobile aerosol research laboratory and data processing tools for effective stationary and mobile field measurements, Atmos. Meas. Tech., 5, 1443–1457, doi:10.5194/amt-5-1443-2012, 2012.

Fenske, J. D., Hasson, A. S., Ho, A. W., and Paulson, S. E.: Measurement of absolute unimolecular and bimolecular rate constants for CH$_3$CHOO generated by the trans-2-butene reaction with ozone in the gas phase, J. Phys. Chem. A, 104, 9921–9932, doi:10.1021/jp0016636, 2000.

Fry, J. L., Draper, D. C., Barsanti, K. C., Smith, J. N., Ortega, J., Winkle, P. M., Lawler, M. J., Brown, S. S., Edwards, P. M., Cohen, R. C., and Lee, L.: Secondary Organic Aerosol Formation and Organic Nitrate Yield from NO$_3$ Oxidation of Biogenic Hydrocarbons, Environ. Sci. Technol., 48, 11944–11953, doi:10.1021/es502204x, 2014.

Geyer, A., Alicke, B., Ackermann, R., Martinez, M., Harder, H., Brune, W., di Carlo, P., Williams, E., Jobson, T., Hall, S., Shetter, R., and Stutz, J.: Direct observations of daytime NO$_3$: Implications for urban boundary layer chemistry, J. Geophys. Res.-Atmos., 108, 3619–3631, doi:10.1016/S1352-2310(00)00549-5, 2003.

Hallquist, M., Wangberg, I., Ljungstrom, E., Barnes, I., and Becker, K. H.: Aerosol and product yields from NO$_3$ radical-initiated oxidation of selected monoterpenes, Environ. Sci. Technol., 33, 553–559, doi:10.1021/es980292s, 1999.

Handisides, G. M.: The influence of peroxy radicals on ozone production, Fachbereich Geowissenschaften, Johann Wolfgang Goethe Universität, Frankfurt am Main, Germany, 2001.

Heintz, F., Platt, U., Flentje, H., and Dubois, R.: Long-term observation of nitrate radicals at the tor station, Kap Arkona (Rugen), J. Geophys. Res.-Atmos., 101, 22891–22910, 1996.

Johnson, D. and Marston, G.: The gas-phase ozonolysis of unsaturated volatile organic compounds in the troposphere, Chem. Soc. Rev., 37, 699–716, doi:10.1039/b704260b, 2008.

Johnston, H. S., Davis, H. F., and Lee, Y. T.: NO$_3$ photolysis product channels: Quantum yields from observed energy thresholds, J. Phys. Chem., 100, 4713–4723, doi:10.1021/jp952692x, 1996.

Lelieveld, J., Butler, T. M., Crowley, J. N., Dillon, T. J., Fischer, H., Ganzeveld, L., Harder, H., Lawrence, M. G., Martinez, M.,

Taraborrelli, D., and Williams, J.: Atmospheric oxidation capacity sustained by a tropical forest, Nature, 452, 737–740, 2008.

Li, J., Reiffs, A., Parchatka, U., and Fischer, H.: In situ measurements of atmospheric CO and its correlation with NO$_x$ and O$_3$ at a rural mountain site, Metrol. Meas. Syst., XXII, 25–38, 2015.

Mao, J., Ren, X., Zhang, L., Van Duin, D. M., Cohen, R. C., Park, J.-H., Goldstein, A. H., Paulot, F., Beaver, M. R., Crounse, J. D., Wennberg, P. O., DiGangi, J. P., Henry, S. B., Keutsch, F. N., Park, C., Schade, G. W., Wolfe, G. M., Thornton, J. A., and Brune, W. H.: Insights into hydroxyl measurements and atmospheric oxidation in a California forest, Atmos. Chem. Phys., 12, 8009–8020, doi:10.5194/acp-12-8009-2012, 2012.

Martinez, M., Perner, D., Hackenthal, E. M., Kulzer, S., and Schutz, L.: NO$_3$ at Helgoland during the NORDEX campaign in October 1996, J. Geophys. Res.-Atmos., 105, 22685–22695, 2000.

McLaren, R., Wojtal, P., Majonis, D., McCourt, J., Halla, J. D., and Brook, J.: NO$_3$ radical measurements in a polluted marine environment: links to ozone formation, Atmos. Chem. Phys., 10, 4187–4206, doi:10.5194/acp-10-4187-2010, 2010.

Mogensen, D., Gierens, R., Crowley, J. N., Keronen, P., Smolander, S., Sogachev, A., Nölscher, A. C., Zhou, L., Kulmala, M., Tang, M. J., Williams, J., and Boy, M.: Simulations of atmospheric OH, O$_3$ and NO$_3$ reactivities within and above the boreal forest, Atmos. Chem. Phys., 15, 3909–3932, doi:10.5194/acp-15-3909-2015, 2015.

Novelli, A., Hens, K., Tatum Ernest, C., Kubistin, D., Regelin, E., Elste, T., Plass-Dülmer, C., Martinez, M., Lelieveld, J., and Harder, H.: Characterisation of an inlet pre-injector laser-induced fluorescence instrument for the measurement of atmospheric hydroxyl radicals, Atmos. Meas. Tech., 7, 3413–3430, doi:10.5194/amt-7-3413-2014, 2014.

Noxon, J. F., Norton, R. B., and Marovich, E.: NO$_3$ in the Troposphere, Geophys. Res. Lett., 7, 125–128, 1980.

Orphal, J., Fellows, C. E., and Flaud, P. M.: The visible absorption spectrum of NO$_3$ measured by high-resolution Fourier transform spectroscopy, J. Geophys. Res.-Atmos., 108, 4077, doi:10.1029/2002JD002489, 2003.

Osthoff, H. D., Pilling, M. J., Ravishankara, A. R., and Brown, S. S.: Temperature dependence of the NO$_3$ absorption cross-section above 298 K and determination of the equilibrium constant for NO$_3$ + NO$_2$ ↔ N$_2$O$_5$ at atmospherically relevant conditions, Phys. Chem. Chem. Phys., 9, 5785–5793, 2007.

Osthoff, H. D., Roberts, J. M., Ravishankara, A. R., Williams, E. J., Lerner, B. M., Sommariva, R., Bates, T. S., Coffman, D., Quinn, P. K., Dibb, J. E., Stark, H., Burkholder, J. B., Talukdar, R. K., Meagher, J., Fehsenfeld, F. C., and Brown, S. S.: High levels of nitryl chloride in the polluted subtropical marine boundary layer, Nat. Geosci., 1, 324–328, 2008.

Ouyang, B., McLeod, M. W., Jones, R. L., and Bloss, W. J.: NO$_3$ radical production from the reaction between the Criegee intermediate CH$_2$OO and NO$_2$, Phys. Chem. Chem. Phys., 15, 17070–17075, doi:10.1039/c3cp53024h, 2013.

Phillips, G. J., Tang, M. J., Thieser, J., Brickwedde, B., Schuster, G., Bohn, B., Lelieveld, J., and Crowley, J. N.: Significant concentrations of nitryl chloride observed in rural continental Europe associated with the influence of sea salt chloride and anthropogenic emissions, Geophys. Res. Lett., 39, L10811, doi:10.1029/2012GL051912, 2012.

Platt, U., Perner, D., Winer, A. M., Harris, G. W., and Pitts, J. N. J.: Detection of NO$_3$ in the polluted troposphere by differential optical absorption, Geophys. Res. Lett., 7, 89–92, 1980.

Presto, A. A. and Donahue, N. M.: Ozonolysis fragment quenching by nitrate formation: The pressure dependence of prompt OH radical formation, J. Phys. Chem. A, 108, 9096–9104, doi:10.1021/jp047162s, 2004.

Riemer, N., Vogel, H., Vogel, B., Anttila, T., Kiendler-Scharr, A., and Mentel, T. F.: Relative importance of organic coatings for the heterogeneous hydrolysis of N$_2$O$_5$ during summer in Europe, J. Geophys. Res.-Atmos., 114, D17307, doi:10.1029/2008JD011369, 2009.

Rinne, J., Markkanen, T., Ruuskanen, T. M., Petäjä, T., Keronen, P., Tang, M. J., Crowley, J. N., Rannik, Ü., and Vesala, T.: Effect of chemical degradation on fluxes of reactive compounds – a study with a stochastic Lagrangian transport model, Atmos. Chem. Phys., 12, 4843–4854, doi:10.5194/acp-12-4843-2012, 2012.

Sarwar, G., Simon, H., Bhave, P., and Yarwood, G.: Examining the impact of heterogeneous nitryl chloride production on air quality across the United States, Atmos. Chem. Phys., 12, 6455–6473, doi:10.5194/acp-12-6455-2012, 2012.

Schuster, G., Labazan, I., and Crowley, J. N.: A cavity ring down/cavity enhanced absorption device for measurement of ambient NO$_3$ and N$_2$O$_5$, Atmos. Meas. Tech., 2, 1–13, doi:10.5194/amt-2-1-2009, 2009.

Stone, D., Blitz, M., Daubney, L., Howes, N. U. M., and Seakins, P.: Kinetics of CH$_2$OO reactions with SO$_2$, NO$_2$, NO, H$_2$O and CH$_3$CHO as a function of pressure, Phys. Chem. Chem. Phys., 16, 1139–1149, doi:10.1039/c3cp54391a, 2014.

Stutz, J., Alicke, B., Ackermann, R., Geyer, A., White, A., and Williams, E.: Vertical profiles of NO$_3$, N$_2$O$_5$, O$_3$, and NO$_x$ in the nocturnal boundary layer: 1. Observations during the Texas Air Quality Study 2000, J. Geophys. Res.-Atmos., 109, D12306, doi:10.1029/2003JD004209, 2004.

Stutz, J., Wong, K. W., Lawrence, L., Ziemba, L., Flynn, J. H., Rappenglueck, B., and Lefer, B.: Nocturnal NO$_3$ radical chemistry in Houston, TX, Atmos. Env., 44, 4099–4106, doi:10.1016/j.atmosenv.2009.03.004, 2010.

Taipale, R., Sarnela, N., Rissanen, M., Junninen, H., Rantala, P., Korhonen, F., Siivola, E., Berndt, T., Kulmala, M., Mauldin, R. L., Petaja, T., and Sipila, M.: New instrument for measuring atmospheric concentrations of non-OH oxidants of SO$_2$, Boreal Environ. Res., 19, 55–70, 2014.

Taraborrelli, D., Lawrence, M. G., Crowley, J. N., Dillon, T. J., Gromov, S., Groß, C. B. M., Vereecken, L., and Lelieveld, J.: Hydroxyl radical buffered by isoprene oxidation over tropical forests, Nat. Geosci., 5, 190–193, 2012.

Thieser, J., Schuster, G., Schuladen, J., Phillips, G. J., Reiffs, A., Parchatka, U., Pöhler, D., Lelieveld, J., and Crowley, J. N.: A two-channel thermal dissociation cavity ring-down spectrometer for the detection of ambient NO$_2$, RO$_2$NO$_2$ and RONO$_2$, Atmos. Meas. Tech., 9, 553–576, doi:10.5194/amt-9-553-2016, 2016.

Thornton, J. A., Kercher, J. P., Riedel, T. P., Wagner, N. L., Cozic, J., Holloway, J. S., Dube, W. P., Wolfe, G. M., Quinn, P. K., Middlebrook, A. M., Alexander, B., and Brown, S. S.: A large atomic chlorine source inferred from mid-continental reactive nitrogen chemistry, Nature, 464, 271–274, doi:10.1038/nature08905, 2010.

Vereecken, L., Harder, H., and Novelli, A.: The reaction of Criegee intermediates with NO, RO$_2$, and SO$_2$, and their fate in the atmosphere, Phys. Chem. Chem. Phys., 14, 14682–14695, doi:10.1039/c2cp42300f, 2012.

Voigt, S., Orphal, J., and Burrows, J. P.: The temperature and pressure dependence of the absorption cross-sections of NO$_2$ in the 250–800 nm region measured by Fourier-transform spectroscopy, J. Photoch. Photobiol. A, 149, 1–7, doi:10.1016/s1010-6030(01)00650-5, 2002.

von Friedeburg, C., Wagner, T., Geyer, A., Kaiser, N., Vogel, B., Vogel, H., and Platt, U.: Derivation of tropospheric NO$_3$ profiles using off-axis differential optical absorption spectroscopy measurements during sunrise and comparison with simulations, J. Geophys. Res.-Atmos., 107, 4168, doi:10.1029/2001JD000481, 2002.

Wayne, R. P., Barnes, I., Biggs, P., Burrows, J. P., Canosa-Mas, C. E., Hjorth, J., Le Bras, G., Moortgat, G. K., Perner, D., Poulet, G., Restelli, G., and Sidebottom, H.: The nitrate radical: Physics, chemistry, and the atmosphere, Atmos. Environ. A-Gen, 25A, 1–206, 1991.

Welz, O., Savee, J. D., Osborn, D. L., Vasu, S. S., Percival, C. J., Shallcross, D. E., and Taatjes, C. A.: Direct kinetic measurements of Criegee intermediate (CH$_2$OO) formed by reaction of CH$_2$I with O$_2$, Science, 335, 204–207, doi:10.1126/science.1213229, 2012.